FINAL REPORT

ADVANCED MICROWAVE SOUNDING UNIT STUDY FOR ATMOSPHERIC INFRARED SOUNDER

NASA Contract No. NAS5-30791

covering the period

March 29, 1990 to January 14, 1992

Submitted by

Philip W. Rosenkranz
David H. Staelin

Massachusetts Institute of Technology
Research Laboratory of Electronics
Cambridge, Massachusetts 02139

August 12, 1992

Contents

1. Introduction

The Atmospheric Infrared Sounder (AIRS), the Advanced Microwave Sounding Unit (AMSU-A) and the Microwave Humidity Sounder (MHS, formerly AMSU-B) together constitute the advanced sounding system facility for the Earth Observing System (EOS). This report is a summary of the EOS "phase B" activities of team members P. W. Rosenkranz and D. H. Staelin, through 1991. Work is continuing in the execution phase.

The principal effort, design of algorithms for retrieval of geophysical parameters, is described in Section 2. Section 3 describes aspects of aircraft-based radiometer measurements that are relevant to AIRS/AMSU. (This experimental program was primarily supported by NASA under a separate grant.) Section 4 is a discussion of calibration issues for AMSU-A and MHS. Since these will be NOAA operational instruments, it is anticipated that calibration algorithms, including antenna pattern corrections, will be made available to the EOS program in a timely way. The team members' efforts in this area include cognizance of these algorithms with respect to AIRS objectives, but not algorithm redefinitions or coding. Appendix A is the Preliminary Execution/Operations Phase Data Plan. Appendix B contains memoranda prepared by team members Rosenkranz and Staelin for the AIRS project.

2. Algorithm Development

2.1 Line-by-line Transmittance Algorithms

Recent laboratory measurements made by Liebe *et al.* (1991) of microwave attenuation in dry air were used to revise the line-mixing coefficients for the 60-GHz band of oxygen. These coefficients pertain to a band shape described by the equation

$$\alpha(\nu) = \frac{n}{\pi} \sum_i S_i \left(\frac{\nu}{\nu_i}\right)^2 \left[\frac{\gamma_i + (\nu-\nu_i) Y_i}{(\nu-\nu_i)^2 + \gamma_i^2} + \frac{\gamma_i - (\nu+\nu_i) Y_i}{(\nu+\nu_i)^2 + \gamma_i^2} \right], \qquad (1)$$

where $\alpha(\nu)$ is the absorption coefficient at frequency ν, n is the number density of $O_2{}^{16}$ molecules, S_i is line intensity, ν_i is line frequency, γ_i is the line broadening parameter, and Y_i is the line mixing parameter. The temperature and pressure dependence of the Y's were modeled by

$$Y_i = (a_5 \theta^{0.8} + a_6 \theta^{1.8})\ P, \qquad (2)$$

where $\theta = 300/T$. The coefficients a_5 and a_6 were fitted by a constrained ridge-regression to the meaasured spectra at 279, 303 and 327K, for 700 hPa pressure. The new coefficients are given by Liebe *et al.* (1992), and were incorporated in a subroutine provided to the TLSCF at JPL in January 1992.

Algorithms for calculation of microwave attenuation by water vapor and by small liquid water droplets have also been sent to the TLSCF.

2.2 Temperature and Moisture Profile Retrieval Algorithm

Figure 2.1 is a block diagram of the overall temperature and moisture profile retrieval processing that we envision for AIRS/AMSU/MHS. This is a recursive algorithm in which the final profiles of temperature and moisture provide initial profiles for the next spot. (Additional discussion of this scheme is contained in the team members' proposal, "Recursive Estimation of Geophysical Products with AIRS/AMSU Data.") AMSU and MHS measurements are processed first, to obtain an intermediate profile (labeled "second profile") which provides the starting point of the AIRS cloud-clearing and retrieval. Variations on the scheme shown in this figure are also possible: for example, stratospheric channels from AIRS for which cloud contamination is minimal could be input to the first retrieval along with AMSU data. However, the instrument-based division of processing shown in the figure offers the opportunity to check for inconsistencies between calibration of the instruments.

Figure 2.2 shows an expanded view of the surface parameter estimation block from the previous figure. Depending on the type of surface, either of the two algorithms shown in Figures 2.3 and 2.4 are applied. The "cryosphere" algorithm, Figure 2.3, is used for non-frozen land as well as ice. The surface brightness model is a three-parameter version of the model of Grody (1988):

$$\varepsilon(\nu)\, T_S = [T_0 + (\nu/\nu_0)^2 T_\infty] \,/\, [1 + (\nu/\nu_0)^2], \qquad (3)$$

where $\varepsilon(\nu)$ is emissivity as a function of frequency ν and T_S is surface temperature. The algorithm uses the four AMSU window channels to solve for the parameters T_0, T_∞, ν_0 and precipitable water vapor. At present, the algorithm does not include liquid water. Hence, precipitation over land will cause some perturbation of the inferred surface

emissivity.

The hydrosphere algorithm, Figure 2.4, is applied over water. The geophysical model includes atmospheric absorption due to oxygen, water vapor, and liquid water clouds, and also surface roughness. The surface emissivity model is of the form

$$\varepsilon(\nu) = \varepsilon_s(\nu,T_s) + [\partial\varepsilon(\nu)/\partial u_*]\, u_*, \tag{4}$$

where $\varepsilon_s(\nu,T_s)$ is smooth-surface emissivity computed using a polynomial approximation to the Klein and Swift (1977) equations, and u_* is surface friction velocity (a measure of wind stress on the surface). The coefficients within the square brackets in Eq. (4) will be determined empirically (e.g., Rosenkranz, 1992). Precipitable water vapor, liquid water and u_* are solved for by the method of iterated minimum-variance. A scattering albedo at 89 GHz is also produced, as a precipitation indicator.

The profile retrieval algorithm (denoted by "retrieval 1" in Figure 2.1), is shown in Figure 2.5. This is an iterative algorithm in which the profile increments are obtained by the minimum-variance method, using weighting functions computed for the temperature profile with a rapid transmittance algorithm. In simulations, two iterations are usually required, starting from a standard profile. The moisture profile can have two components, vapor and liquid, depending on whether the vapor at a given level is at the saturation value. The reapportionment block at the bottom of this figure is expanded in Figure 2.6. This algorithm converts any vapor that exceeds the saturation value to liquid. The conversion factor is a function of temperature that has not yet been determined.

2.3 Algorithms for Research Products

2.3.1 Sea-Ice Cover and Land Snow/Ice Cover Index

These algorithms have similar architecture. Both employ point operators on the AMSU-A brightness temperatures (for 50-km horizontal resolution) and/or MHS brightness temperatures (for 15-km resolution). Auxiliary inputs to the algorithms are: land/sea flag, land elevation, latitude, longitude, and estimated surface temperature. The point operators are of the form

$$C_i = \Sigma\, a_{ijklm}\, B_j^{\,l}\, B_k^{\,m}, \tag{5}$$

with

$$\underline{B} = \mathbf{D}\,\underline{A}, \tag{6}$$

where **D** is a matrix (possibly selected from a library) and **A** is a vector of selected parameters (e.g. brightness temperatures).

2.3.2 Precipitation Index

This algorithm employs, in addition to point operators as discussed above, area operators of the form

$$H = F_\theta * G \tag{7}$$

operating in an area A = ac, where a is the length of a block of data along the satellite track and c is the swath width; G and H are 1-D or 2-D scalar fields, F_θ is a filter function dependent on the scan angle θ, and * denotes the convolution operation. The auxiliary inputs to the algorithm will be the land/sea flag, land elevation, and adjacent estimates of surface temperature and temperature and humidity profiles. Figure 2.7 illustrates the detection of a precipitation signal in AMSU data.

The theoretical calculations on which the precipitation algorithm will be based include the following assumptions:

spherical hydrometeors, water or ice,
Mie scattering,
planar-stratified atmosphere and clouds,
reduced phase matrix - asymmetric, two Stokes' parameters,
discrete angles (~8) and levels (~ 40),
iterative calculations,
various size distributions - e.g. Marshall-Palmer,
climatology - to be determined.

Figure 2.8 shows that of those rain cells observed during the GALE and COHMEX missions their "microwave" diameters exceeded 50 km for approximately one-third of the cells, i.e. AMSU would resolve them. Since these cell diameters substantially exceed the thickness of these storms, the laminar approximation seems appropriate. At worst, the laminar structure might not fill an entire beam.

Figure 2.9 makes another point. It shows that microwave spectra observed near oxygen absorption bands can vary markedly, but with only two or three observable degrees of freeedom, i.e., since the observed spectra vary in such simple ways, overly complex

physical models may not be relevant. Figure 2.10 shows the absorption and scattering cross sections for rain and ice at a much wider range of frequencies. Again, the spectra are very simple in form and few degrees of freedom suffice to represent them quite well.

In Figure 2.11, we see comparisons between the brightness temperatures observed during COHMEX at 53.65 GHz and 118.75 GHz. This distribution correlates very well with the distribution of the brightness temperatures predicted by the simple proposed scattering model and the equation of radiative transfer. This point is made even more strongly in Figure 2.12, where the two degrees of freedom for the observed 118-GHz spectra, labeled here Mode 1 and Mode 2. are shown to agree very well with the same parameters predicted using these simple scattering models based on parameters inferred from CP-2 radar observations during this particular flight..

In conclusion, the simple assumptions made for the scattering model to be used in AMSU simulation computations appears to be sufficiently accurate given the limited degreees of freedom of the observations and their ability to be approximated well by the models suggested here.

3. Aircraft-based Measurements

During the Convection and Precipitation/Electrification (CaPE) experiment, a suite of instruments on the NASA ER-2 high-altitude aircraft made measurements that simulated the types of data that will be obtained from EOS. MIT provided the Millimeter-wave Temperature Sounder (MTS), which is a dual-band, 52-54 and 119 GHz, radiometer. This system is capable of either down-looking or up-looking observations. In the down-looking mode, particular interest attaches to the response of MTS to hydrometeors; this data will be useful in understanding future AMSU measurements of precipitation. The up-looking mode can be used to test theoretical expressions (such as described in Section 2.1) for atmospheric transmittance.

The CaPE experiment was conducted during July and August 1991. Table 3.1 summarizes the flights and gives the approximate amount of data obtained with MTS. Numerous problems with intermittent cable connections and a defective I/O board in the computer resulted in complete loss of data from five flights. When data was recorded, it was usual for a few of the nine channels to be inoperative. Despite these difficulties, some data was obtained from nine flights. Since there is a great deal of redundancy among the eight channels at 118.75 GHz, most of this data is, in principle, interpretable. The 53 GHz channel, however, exhibited instabilities that appear to have made this channel unusable. Among the observations of precipitating cloud systems, the most noteworthy were two

overflights of Hurricane Bob on August 19. These high-resolution measurements of a hurricane are unique at these wavelengths. The more transparent channels show large perturbations from the clouds, while the higher-peaking channels respond to temperature variations (on isobaric surfaces). The measurements form Hurricane Bob are currently being analyzed, and a paper will be prepared for publication.

Following the CaPE experiment, significant improvements in reliability and performance of the MTS were achieved as a result of modifications to the 53-GHz front-end subsystem and in the back-end/computer subsystem. Flights in 1992 (STORMFEST) have demonstrated reliable operation of the instrument.

Table 3.1

1991 CAPE flight summary - MTS

date	hrs. of recorded data	viewing	comments
7-21	5	up	
7-24	0		
7-28	0		
7-30	1	down	pre-convective moisture
8-1	0		
8-5	6	down	thunder storms over land
8-6	1	down	no cal.
8-8	0		
8-12	7	up	
8-13	2	up	
8-16	0		
8-17	6	up	
8-19	2	down	Hurricane Bob
8-21	6	down	trace gas net.

4. Calibration of AMSU and MHS

4.1 Introduction

This section defines principles and procedures for calibration of the AMSU and MHS instruments. Subsections 4.2 to 4.4 deal with the prelaunch procedures in three categories: radiometric calibration, which is the determination of the relation betwen the input mean brightness temperature (i.e. as from a uniform black-body radiating environment) and the output counts from each channel of the instrument; spectral calibration, which is the relative response of each channel to input brightness as a function of frequency; and directivity calibration, which is the relative response of each channel to input brightness as a function of angular coordinates and polarization. Subsection 4.5 deals with issues of cross-calibration between AMSU and MIMR. These procedures are postlaunch and relate primarily to radiometric calibration, spectral and directivity calibration being a prerequisite.

4.2 Radiometric Calibration

Both AMSU and MHS will employ two-point external calibration sequences: the antenna reflectors will rotate from the earth to cold space to an on-board target. Conceptually, this method of calibration is simple and straightforward; the critical issues are related to departures of the instrument response from linearity between the two calibration points, and to the deviation of the on-board target from unity emissivity. (Stray radiative energy impinging on the sidelobes of the antennas when they view the target or space is also an issue, but we consider this to be part of directivity calibration.)

In the absence of nonlinearity, the radiometer calibration equation would be

$$I_A = I_C + (V_A - V_C)\ (I_H - I_C)\ (V_H - V_C)^{-1} \qquad (8)$$

where I_A is the radiometric input intensity, usually expressed in degrees Kelvin, I_C and I_H are the radiometric intensities of the two calibration points (distinguished from their physical temperatures as discussed below), and V_A, V_C, V_H are the corresponding radiometer outputs (counts).

Departures from linearity are expected to be small, so we will assume that the radiometer output can be represented by a quadratic function of the pre-detector power level, which in turn is proportional to the sum of the input radiometric intensity I_A and the radiometer noise temperature referenced to the input, T_N. Hence

$$V_A = V_0 + g\,(I_A + T_N) + \beta\,[g\,(I_A + T_N)]^2 \qquad (9)$$

where V_0, g and β are coefficients that characterize the instrument response. V_0 can be eliminated by taking

$$(V_H - V_C) / (I_H - I_C) = g\,[1 + \beta\, g\,(2T_N + I_H + I_C)]. \qquad (10)$$

A similar equation exists in which I_A is substituted for I_H; thus

$$I_A = I_C + (V_A - V_C)\,(I_H - I_C)\,(V_H - V_C)^{-1}\,[1 + \beta\, g\,(2T_N + I_H + I_C)]\,[1 + \beta\, g\,(2T_N + I_A + I_C)]^{-1}, \qquad (11)$$

instead of Eq. (8). Now, if we retain only terms of first order in β, Eq. (11) simplifies to

$$I_A = I_C + (V_A - V_C)\,(I_H - I_C)\,(V_H - V_C)^{-1}\,[1 + \beta\, g\,(I_H - I_A)]. \qquad (12)$$

Since g is multiplied by β on the right side of Eq.(12), we can to the same order of accuracy approximate $g\,(I_H - I_A)$ by $(V_H - V_A)$:

$$I_A = I_C + (V_A - V_C)\,(I_H - I_C)\,(V_H - V_C)^{-1}\,[1 + \beta\,(V_H - V_A)]. \qquad (13)$$

With two calibration points, β cannot be determined in orbit; it can be measured in pre-launch test with a variable-temperature "earth target," by fitting Eq. (13) to measurements of V_A as a function of I_A. We can deduce from Eq. (12) that if the maximum effect of the βg-term (with I_A midway between the calibration points $I_C = 3$ K and $I_H = 300$ K, which implies $(V_A - V_C)(V_H - V_C)^{-1} = 0.5$) were to be as large as 0.5 K, then $\beta g \sim 2 \cdot 10^{-5}\ K^{-1}$. In Eq. (9) the ratio of the quadratic to the linear term is $\beta g(I_A + T_N)$; even for a rather low T_N of 500 K, the system nonlinearity with $I_A = 300$ K would then be ~ 1.5 %, which would exceed specifications. Hence a significant nonlinearity of the radiometer response in the overall system tests would imply a faulty instrument.

The radiometric intensities that were used in the above calibration equations can be different from physical temperatures for three reasons. First, for an ideal black body at a temperature T we have

$$I = (h\nu/k)\,[\exp(h\nu/kT) - 1]^{-1}. \qquad (14)$$

In the (Rayleigh-Jeans) limit $\nu/T \rightarrow 0$, $I = T$; even at most microwave frequencies, the difference between I and T amounts to a constant offset that usually is ignored. However, at the high frequencies of the MHS, T - I is significantly different for cold space than for higher temperatures.

Second, the onboard calibration target is not an ideal black body. Since the reflector is very close to the target when observing it, radiant energy reflected from the target will originate mostly from parts of the instrument at similar temperatures. Target emissivity might therefore not be a critical issue, except for the fact that the output response of a radiometer can be affected by the standing-wave ratio at its input. This sensitivity can be determined by replacing the radiometer antenna with a tunable short and measuring the change in radiometer output as the position of the short is varied. This is a type of standing-wave measurement, in which the wave generator is the local oscillator. Since the radiometer has a square-law detector, the measurement can be described with a power standing-wave ratio,

$$PSWR = (1 + |\Gamma|)^2 / (1 - |\Gamma|)^2 = 1 + \Delta I_A / (I_A + T_N) \qquad (15)$$

where Γ is a complex amplitude reflection coefficient and ΔI_A is the peak-to-peak variation of calibrated radiometer output observed in the tunable-short test. Γ includes factors due to coupling into the mixer, isolation between the mixer and the short, as well as the reflection coefficient of the short itself, which has unit amplitude but variable phase. For the present discussion, we need only note that these factors imply $|\Gamma| << 1$; hence, to first order,

$$PSWR \approx 1 + 4|\Gamma| \qquad (16)$$

and $|\Gamma|$ is therefore proportional to ΔI_A by Eq.(15).

When the tunable short is replaced by the antenna, the value of Γ is reduced in proportion to the amplitude of the return wave, to a value Γ_A. The reflected wave from the target may in fact be overwhelmed by a wave from the antenna reflector, part of which lies very close to the edge of the feed horn. It is important to note that the wave component that is significant in the calibration problem is the one that varies with antenna position. Because the polarization is linear, the signal reflected back into the horn by the reflector will be dependent on the antenna pointing direction. The in-orbit calibration error ΔI expected with a given value of the tunable short variation ΔI_A is

$$\Delta I = r_A \, \Delta I_A \, , \tag{17}$$

where

$$r_A = 0.5 \max_{i,j} \, |\Gamma_A(i) - \Gamma_A(j)| \tag{18}$$

and $\Gamma_A(i)$ is the complex amplitude reflection coefficient of the antenna at position i. Equation (18) incorporates only the variable reflection from the antenna, which, because it is position-dependent, is not removed by the calibration algorithm. One way to ascertain the level of this reflection is to measure carefully the VSWR's and the standing-wave-pattern null locations of a representative complete antenna horn assembly in the laboratory as the antenna rotates to all possible positions, including calibration positions. Such measurements should be made at both the local oscillator frequency and its second harmonic.

These errors can vary over portions of an orbit as instrument temperatures, voltages, and dimensions vary, and so they are potentially very pernicious. Let us assume that a tolerable calibration error from this effect is ± 0.3 K, or 0.6 K peak-to-peak. Such random 0.3K errors in the hot and cold calibration measurements and in the atmospheric observation can combine to yield noise-free calibrated observation errors of 0.6K. For a reflected local oscillator wave of -30 dB (r_A= 1/32 in amplitude), ΔI_A in the tunable short test should be less than 0.6 K · 32 = 19 K peak-to-peak.

The third potential reason for differences between radiometric intensities and the physical temperatures of calibration points is radiant energy from a source at a different temperature, either on the spacecraft or elsewhere, entering the antenna sidelobes. These contributions can be simulated in a test chamber with a mockup of the spacecraft.

4.3 Spectral Calibration

The radiometer responds to a weighted average of the input intensity $I_A(\nu)$,

$$I_A = \int I_A(\nu) \, F(\nu) \, d\nu \, / \int F(\nu) \, d\nu, \tag{19}$$

where $F(\nu)$ is the spectral response function of the radiometer. Generally, the variation of $F(\nu)$ with ν is set by the I.F. filters, and if the first radiometer stage is a mixer, the two passbands are very nearly symmetric about the local oscillator frequency. Departures from symmetry can be caused by the impedance match of the mixer and I.F. amplifiers varying over the range of frequencies received.

Ideally, F(ν) consists of one or more rectangular passbands. As a practical matter, the geophysical algorithms will almost certainly incorporate weighting functions computed for these ideal passbands. Otherwise, their coefficients would all be instrument-dependent. If I(ν) were independent of frequency, of course, then the measurement would be unaffected by the relative shape of the instruments' passbands. Hence the effect of departures from the ideal passband shape is observation-dependent. Given an ensemble of atmospheric profiles, a particular response function F(ν) will generate the error $\varepsilon = I_A - I_A^*$, where I_A^* is the average intensity corresponding to ideal rectangular passbands. Then ε will have some average value over the ensemble, and a variable component. The average value of ε can be treated as a calibration offset, and compensated. The variable component in ε would then contrbute to the error budget. This source of error should be held to a few tenths of a Kelvin, which is the basis for specifications of maximum passband ripple or asymmetry.

4.4. Directivity Calibration

The power intensity $I_A(\nu)$ input to the instrument is related to the incident intensity $I_p(\Omega,\nu)$ by

$$I_A(\nu) = (4\pi)^{-1} \sum_{p=0}^{3} \iint I_p(\Omega,\nu)\, D_p(\Omega,\nu)\, d\Omega, \qquad (20)$$

where the index p denotes the Stokes parameters (p = 0 for total intensity, etc.; see Kraus, 1966) and $D_p(\Omega,\nu)$ is the directive gain function of the antenna, which is normalized so that

$$\iint D_0(\Omega,\nu)\, d\Omega = 4\pi, \qquad (21)$$

where the integrations are carried over all solid angles Ω.

Equation (20) shows that when the scene intensity viewed by the instrument is polarized, which applies to those channels that are sensitive to the surface, then knowledge of the polarization characteristics of the antenna is necessary. The usual measurements of power in two orthogonal polarizations (e.g. P(0°) and P(90°)) do not suffice to determine all four Stokes parameters. With a third measurement P(45°), the first three Stokes parameters can be calculated in unnormalized form as

$$D_0 = P(0°) + P(90°) \tag{22a}$$

$$D_1 = P(0°) - P(90°) \tag{22b}$$

$$D_2 = 2P(45°) - P(0°) - P(90°). \tag{22c}$$

The coordinate system used for antenna measurements can subsequently be converted to a geodetic coordinate system by a rotation. The magnitude of D_3 (circular polarization) can also be determined from this set of three measurements by making use of the fact that as a deterministic system, the antenna is completely polarized; hence

$$D_3^2 = D_0^2 - D_1^2 - D_2^2. \tag{22d}$$

However, AMSU and MHS do not have channels that measure emission from the mesosphere, and therefore one can exclude any significant I_3.

Associated with the directive gain function $D_0(\Omega)$ are the beamwidth θ_{HP} which is the angular distance in a given plane betwen the half-power points; and beam efficiency,

$$\varepsilon_M = (4\pi)^{-1} \iint_{\substack{\text{main} \\ \text{lobe}}} D_0(\Omega,\nu)\, d\Omega, \tag{23}$$

where "main lobe" denotes a cone of angular diameter 2.5 times the beamwidth.

It is desirable that measurements of $D_p(\Omega,\nu)$ should have a dynamic range extending from the maximum value $D = \max(D_0(\Omega))$ to a level such that the unknown contribution to I_A from lower levels cannot exceed a small value, such as 1 K. For I_0 = 300 K, that level would be -25 dB. A rough estimate of D is given by $(229° / \theta_{HP})^2$. For AMSU-A, with a beamwidth of 3.6°, D ≡ 36 dB; hence a dynamic range of 61 dB would be required. For MHS, with θ_{HP} = 1.1°, D ≡ 46 dB and a dynamic range of 71 dB would be needed. Unfortunately it is very difficult to measure antenna patterns accurately over such large dynamic ranges. The relative measurements of $D_0(\Omega)$ could be calibrated by an absolute determination of D, and Eq. (21) then could be used to calculate the fraction of total power from $D_0(\Omega)$ below the noise level of the relative measurements. However, the absolute measurement of D would be required to have an accuracy of ±1/300, or ± 0.015 dB, which

is unattainable.

For the above reasons, it is desirable to supplement the usual pattern measurement with a radiometric measurement of ε_M or of the integrated power within some larger solid angle within which the relative antenna pattern is known. The fraction of power contributed from $D_0(\Omega)$ below the noise level of the pattern measurement can then be estimated. This type of measurement can be done by cutting a circular hole in a large sheet of absorbing material and placing it so that the opening subtends the solid angle of the measurements, and other lines of sight from the instrument are intercepted by absorbers at the same temperature. Thermal contrast is obtained by viewing a tank of liquid nitrogen with absorber at the bottom or (for window channels) the sky through the hole.

4.5 Cross-Calibration of AMSU-A with MIMR

AMSU and MIMR have different fields of view, viewing angles, frequencies, and polarizations, as shown in Figure 4.1. Note that only the channels near 23.8, 31.4, and 89 GHz are comparable. Of most serious concern is the difference between the MIMR channel at 36.5 GHz and AMSU at 31.4 GHz. Also note that the footprints are vastly different, being approximately 10 km in the case of MIMR and 50 km at nadir for AMSU.

Figure 4.2 shows that the frequency difference between the two instruments, 31 GHz and 36 GHz, can correspond to perhaps 10 K of brightness temperatures betwen these two channels. However, note that for a wide variety of meteorological conditions this gradient between the two brightness temperatures does not vary more than a few degrees.

Figure 4.3 suggests the impact of viewing angle. Note the brightness temperatures for certain polarizations can differ by 30 K or more for incidence angles of 30° and 50° (ray angles from zenith). This is for smooth soil, however, one of the worst situations. At wavelengths shorter than the 21 cm pictured here, the angle and polarization dependencies are less. Furthermore, the angular dependence can be estimated to first order by noting the difference in brightness between vertical and horizontal polarization measured by MIMR. Figure 4.4 illustrates the same phenomena for another worst case, ocean. Although these data are also for lower frequencies than those observed by AMSU, the phenomena are somewhat similar, although less marked. Therefore, cross-calibration will require averaging many data points, each corrected for the differences between the two instruments. These differences are mildly nonlinear.

One simple approach to detecting drifts between the calibration constants for the two instruments is then suggested: linear regression between the two sets of observed

brightness temperatures, where these brightness temperatures are observed at the same points, but with the associated fixed differences in viewing angle, frequency, and polarization. The brightness temperature T_{B1} for the first instrument, predicted from the measured T_{B2} for the second instrument, would be

$$T_{B1} = D_{12}\, T_{B2}. \tag{24}$$

Then calibration drift will be evident if D_{12} is based on data in one time period and the observations are from another. Coincidence between angles, spots and climates would improve accuracy. Nonlinear effects can be accommodated by regressing instead the observed brightness tempeatures against those predicted for that same instrument based on the physical parameter retrievals of the second instrument.

$$T_{B1} = D_{12}\, T_{B1}^{P}, \tag{25}$$

where T_{B1}^{P} is computed nonlinearly from the geophysical parameters estimated by instrument 2.

References

Gasiewski, A. J. T., Atmospheric Temperature Sounding and Precipitation Cell Parameter Estimation Using Passive 118-GHz O_2 Observations, Ph.D. Thesis, Dept. of Elec. Eng and Comp. Sci., MIT, Cambridge, MA, Dec. 1988.

Grody, N. C., Surface Identification Using Satellite Microwave Radiometers, *IEEE Trans. Geosci. and Remote Sensing*, vol. 26, 850-859 (1988).

Hollinger, J. P., Passive Microwave Measurements of Sea Surface Roughness, *IEEE Trans. Geosci. Electron*, vol. GE-9, 165-169 (1971).

Klein, L. A., and C. T. Swift, An Improved Model for the Dielectric Constant of Sea Water at Microwave Frequencies, *IEEE Trans. Antennas Propagat.*, vol. AP-25, 104-111 (1977).

Kraus, J. D., Radio Astronomy, (McGraw-Hill,Inc., New York, 1966).

Liebe, H. J., G. A. Hufford, and R. O. DeBolt, The Atmospheric 60-GHz Oxygen Spectrum: Modeling and Laboratory Measurements, NTIA Rpt 91-272, March 1991.

Liebe, H. J., P. W. Rosenkranz, and G. A. Hufford, Atmospheric 60-GHz Oxygen Spectrum: New Laboratory Measurements and Line Parameters, *J. Quant. Spectrosc. Radiat. Transfer* (in press, 1992).

Rosenkranz, P. W., Rough-Sea Microwave Emissivities Measured with the SSM/I, *IEEE Trans. Geosci. and Remote Sensing* (in press, 1992).

Stogryn, A., The Apparent Temperature of the Sea at Microwave Frequencies, *IEEE Trans. Antennas and Propagat.* vol. AP-15, 278-286 (1967).

Appendix A

Preliminary Execution/Operations Phase Data Plan for the Advanced Microwave Sounding Unit

A.1 Introduction

The AIRS Science Team members will generate algorithms and provide the Team Leader Science Computing Facility (TLSCF) with documented prototype software which can be used by TLSCF programmers to produce the operational software package. Because definition of the EOS program remains fluid, and because detailed integration of the AMSU/MHS and AIRS infrared data reduction plans is incomplete, this document is subject to further revision.

A.2 Input Requirements

Inputs to the geophysical algorithms will be: (1) the prior AIRS retrieval of temperature and humidity profiles, including surface temperature; (2) all AMSU/MHS brightness temperatures; (3) a land/water flag; (4) surface elevation; (5) latitude and longitude; (6) scan position; and (7) spacecraft roll, pitch, and yaw. Current AIRS radiances are incorporated in a subsequent processing step performed on the outputs of the algorithms described here.

A.3 Algorithms

Parameter	Nature of Algorithm
initial temperature profile	iterated matrix minimum-variance
initial humidity profile	iterated matrix minimum-variance
cloud liquid water	iterated matrix minimum-variance
sea-ice cover	polynomial/matrix
land snow/ice cover	polynomial/matrix/discriminants
precipitation intensity index	polynomial/matrix & spatial filtering

Transmittance algorithms for AMSU/MHS frequencies, incorporating the results of recent laboratory measurements, were delivered to the TLSCF in August 1991 and updated January 1992. Updates will be provided as appropriate; NASA ER-2 aircraft observations are expected to provide more definitive parameters before 1995.

A.4 Processing Requirements

A.4.1 Calibration Algorithm

The NOAA calibration algorithms for AMSU/MHS will be used for EOS. Revised thermal-vacuum calibration coefficients and antenna pattern corrections are to be provided by the instrument vendor.

A.4.2 Geophysical Algorithm

The algorithm equations are discussed in Section 2. Initial simulations of the temperature and humidity profile retrieval algorithms have been run on an Apollo DN 3500, which is a 0.3 Mflops workstation. A test of 100 profiles ran in 140 seconds when only temperature was retrieved; the humidity retrieval adds ~30% to the run time. This implies the equivalent of 0.6 Mflop per retrieval. (Computation requirements for the other parameters will be much less.) At 50 km resolution, 3.75 spots are observed per second; thus the processing rate would be 2.3 Mflops. However, most of these retrievals required two iterations, whereas with real data sequential profiles will be very similar; thus we expect that the average number of iterations will be close to one. Because these estimates are heavily dependent upon the number of iterations required, more precise estimates must await future study. Presently estimated lines of executable source code for the AMSU portion of the retrieval package are 2000, and approximately 1 Mbyte of memory will be used for storage of constants.

A.5 Output Products

The geophysical parameters produced by SCF will be: (1) temperature profile (degrees K) at ~60 levels; (2) humidity profile (molecules/cm^2) at the same levels; (3) cloud liquid water (kg/m^2) (over water surface); (4) numeric index of precipitation intensity, radiometric mm hr^{-1}; (5) sea ice cover (fraction), ice age index, and indicated salinity; (6) land snow-ice cover (yes/no; index). Data quality indicators will be associated with each parameter.

These data will be produced at the rate of 120 Mbyte/day (nominally 50-km resolution). Formats and media for the standard output products will be set by CDHF. Additionally a 15-km product may be provided, based upon the MHS data, but this remains to be determined.

A.6 Validation Data

Algorithm testing, prior to launch of EOS, will make use of data from NOAA satellites and NASA aircraft. Validation of products and parameters will be done with the data sources listed in Table A1. In the case of the temperature and humidity profiles, there will also be a standard output product from AIRS/AMSU which will be validated by the AIRS team by comparison with radiosondes. Testing and validation of AMSU data will be done on datasets of limited extent, perhaps on the order of 30 days altogether, and will include consistency checks with AIRS clear-air optical retrievals. Cryospheric and precipitation algorithms will be tested in part using AMSU data available from NOAA satellites.

A.7 Simulation Data

A prescription for generating simulated AMSU/MHS data will be provided in support of AIRS/AMSU/MHS software system testing and evaluation.

A.8 Documentation

The theoretical basis of algorithms, software specifications and test procedures will be documented in compliance with AIRS project requirements. Modularity will also support portability and maintainability.

A.9 Algorithm Development Schedule

The schedule is given in Table A2. This schedule is based on the assumption of a December 2000 launch. Since the algorithm can be tested on NOAA satellite and aircraft data prior to EOS launch, it is anticipated that no significant postlaunch changes will be necessary, although some coefficients may be revised.

Table A1 Validation data sources

Parameter	Type of Product	Validation Method
Microwave transmittance	model	ER2 flights
AMSU/MHS TB's	instrumental	calculation from RAOBS
Temperature profile	intermediate	consistency with AIRS*
Humidity profile	intermediate	consistency with AIRS*
Cloud-liquid content	standard (lev. 2)	1. internal consistency 2. MIMR comparison
Sea-ice cover and Land snow-ice cover	standard (lev. 2)	1. AIRS; clear-sky conditions 2. MIMR comparison
Precipitation index	nonstandard (intermediate)	radar

* AIRS/AMSU retrievals of temperature and humdidity profiles will be validated by comparision with radiosondes.

Table A2 Algorithm Development Schedule

Algorithm Development	Jan. 91 - Apr. 98
Documentation	Jan. 91 - Jan. 97
Develop product validation plans	Sept. 93 - Dec. 99
Deliver requirements description	Dec. 91
Deliver detailed description for architectural design	Oct. 94
Deliver prototype code	Apr. 96
Deliver test scenarios	Apr. 97
Deliver expected output specifications, validation	Apr. 98
EOS launch	Dec. '00
Mission operations and data analysis	Dec. '00 - Dec. 2004

Appendix B

MEMORANDUM

To: AIRS Project

From: Philip Rosenkranz

Date: March 7, 1991

Subject: Simulation of clouds for AIRS and AMSU

The Crone algorithm for producing simulations of cloud fields was discussed at the last AIRS team meeting in Pasadena. This model generates the three-dimensional envelope (i.e. the shape) of the clouds. Except for a thin cirrus layer, the clouds are assumed to be opaque at infrared wavelengths. Microwaves, however, will penetrate clouds to some extent, so it will also be necessary to specify the contents of the clouds. In doing this, one should distinguish between the Rayleigh and the Mie regions in drop sizes, and between liquid and ice.

The boundary between applicability of the Rayleigh, or small-droplet, approximation and the exact Mie theory is frequency dependent. At 30 GHz, the Rayleigh approximation underestimates extinction by ~20% for liquid droplets of 200 μ radius, while at 300 GHz, the corresponding upper limit would be 50 μ. (See Figures 5-42 and 5-43 of Chahine *et al.*, 1983.) This range of frequencies roughly encompasses the AMSU channels, so the Rayleigh approximation will be limited to fair-weather clouds. Within the range of validity of this approximation, scattering from liquid droplets is at least an order of magnitude less than absorption; thus the non-scattering equation of radiative transfer can be used. The absorption coefficient can be computed from a model such as the one formulated by Liebe *et al.* (1989). The Rayleigh absorption depends on only a single parameter of the drop-size distribution, which is the mass density.

The boundary between liquid water and ice in clouds can be treated as a temperature threshold. Liquid droplets can be supercooled to a temperature as low as -40 C; however, a more typical lower bound is -10 C. Ice has a smaller dielectric constant than liquid water, and consequently much less absorption; see, e.g., Table 1 of Liebe *et al.* For the small particles of ice in fair-weather clouds, scattering can also be neglected. Hence, the

simulation of these clouds needs to specify the density of liquid water, but not ice.

Table 5-7 of Chahine *et al.* lists 19 different cloud and precipitation models. From this table, one can deduce the following typical values of liquid-water density for fair-weather clouds:

stratus:	0.15 g/m^3
low stratus or stratocumulus:	0.25 g/m^3
cumulus:	0.5 g/m^3

These three values should provide a realistic range in the simulation. Within the clouds, whether liquid or ice, the relative humidity should be set to 100%.

When precipitation is present, the Mie theory should be used to calculate extinction and scattering. This statement applies to both the liquid and ice components; the cirrus anvils associated with thunderstorms produce observable scattering at 89 GHz and higher frequencies. Scattering should also be included in the radiative transfer calculations, as in Gasiewski and Staelin (1990). For the simulation of these clouds, one might choose from Table 5-7 of Chahine *et al.* the steady rain (3 mm/hr), cumulus with rain (12 mm/hr), and cumulonimbus with rain (150 mm/hr) models. These models include coefficients necessary to specify the entire distribution of drop sizes.

The simulation problem can be approached in stages, where the first stage would be clear atmospheres, the second would involve only fair- weather clouds, and the third would include some precipitation. Software to do the calculations of absorption, scattering and radiative transfer discussed above can be supplied to the AIRS project by MIT.

References

Chahine, M. T., D. J. McCleese, P. W. Rosenkranz and D. H. Staelin, "Interaction mechanisms within the atmosphere," Ch. 5 in Manual of Remote Sensing (2nd ed.), Am. Soc. of Photogrammetry, 1983.

Gasiewski, A. J. and D. H. Staelin, "Numerical modeling of passive microwave O_2 observations over precipitation," Radio Sci. 25, 217-235, 1990.

Liebe, H. J., T. Manabe and G. A. Hufford, "Millimeter-wave attenuation and delay rates due to fog/cloud conditions," IEEE Trans. Antenn. Prop. 37, 1617-1623, 1989.

MEMORANDUM January 9, 1992

To: H. H. Aumann
From: P. W. Rosenkranz and D. H. Staelin
Subject: Use of AMSU-A2 module channels in AIRS geophysical product generation

---

The AMSU-A instrument comprises two modules: A1 contains the oxygen-band (temperature) channels and the 89-GHz window channel; A2 contains the 23.8-GHz water channel and the 31.4-GHz window channel.

Use of the A2 channels in generation of AIRS standard products. The way in which the 23- and 31-GHz channels are used depends on the type of surface. Over ocean, these channels are used to derive total precipitable water vapor and total liquid water (clouds). In addition to being a standard product itself, total water vapor provides a tie point or constraint for the humidity profile that is obtained from MHS and AIRS. It also provides a necessary correction for AIRS measurements of surface temperature. Over land or ice surfaces, the 23-, 31-, 50- and 89-GHz channels are used in combination to infer the surface emission spectrum, which is used in both the AMSU temperature and MHS moisture profile retrievals. Total water vapor cannot be derived from these channels over land, and therefore the MHS moisture profile in lower atmospheric levels (pressure > 800 mbar) is 20 to 30% less accurate.

MIMR could serve as a partial substitute for AMSU-A2; however, MIMR has a narrower swath than AMSU, 1400 vs 2200 km. A further incompatibility results from the 50° fixed incidence angle of MIMR, as opposed to the variable incidence angle of AMSU/MHS/AIRS. The surface emission spectrum depends (in general) on incidence angle, and therefore some *ad hoc* assumptions about this dependence would have to be introduced in order to use MIMR data.

In terms of overall objectives, AIRS, AMSU and MHS are intended to function together as a sounding system that can eventually migrate to a NOAA platform. Deletion of any module would be a deficient strategy because it would diminish the demonstration of the potential of this system.

Use of the A2 channels in generation of AIRS research products. Over the ocean, the total water vapor product derived from the 23- and 31-GHz channels provides a correction term for estimation of rain from the 90 GHz channel, which would otherwise suffer from confusion with vapor, particularly in the tropics. (The 90-GHz channel is as sensitive to vapor as the 23-GHz, but several times more sensitive to liquid water, with respect to both absorption and scattering.) Over land, the spectral gradient of emission in the 23 to 31-GHz range is used as an indicator of snow cover.

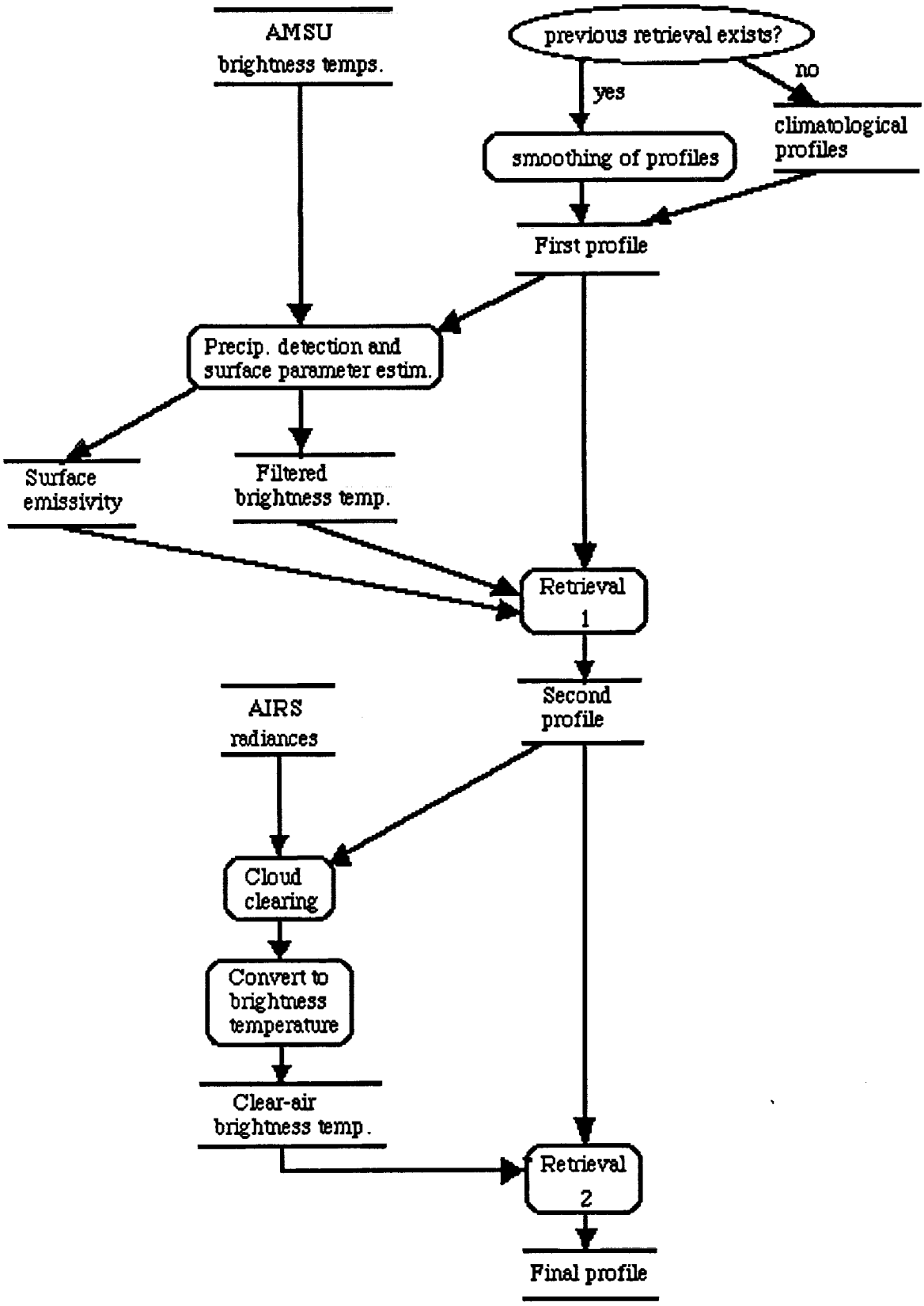

Figure 2.1. AIRS/AMSU profile retrieval.

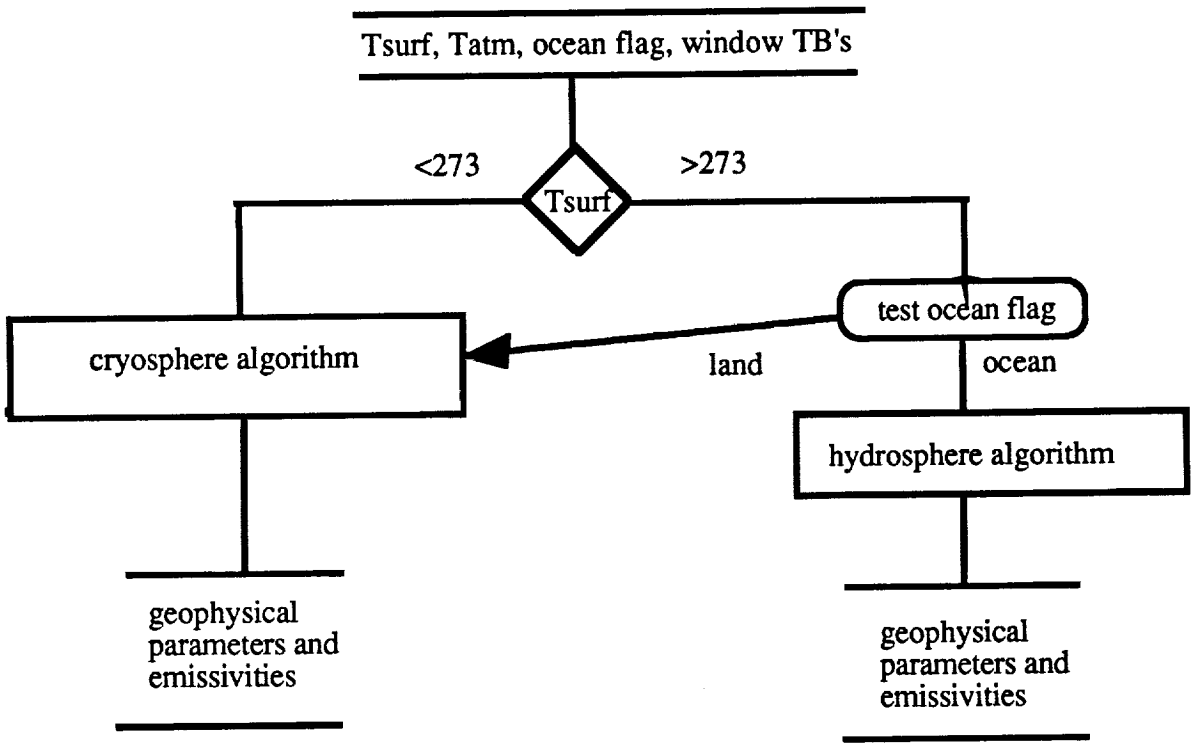

Figure 2.2. Surface parameter estimation.

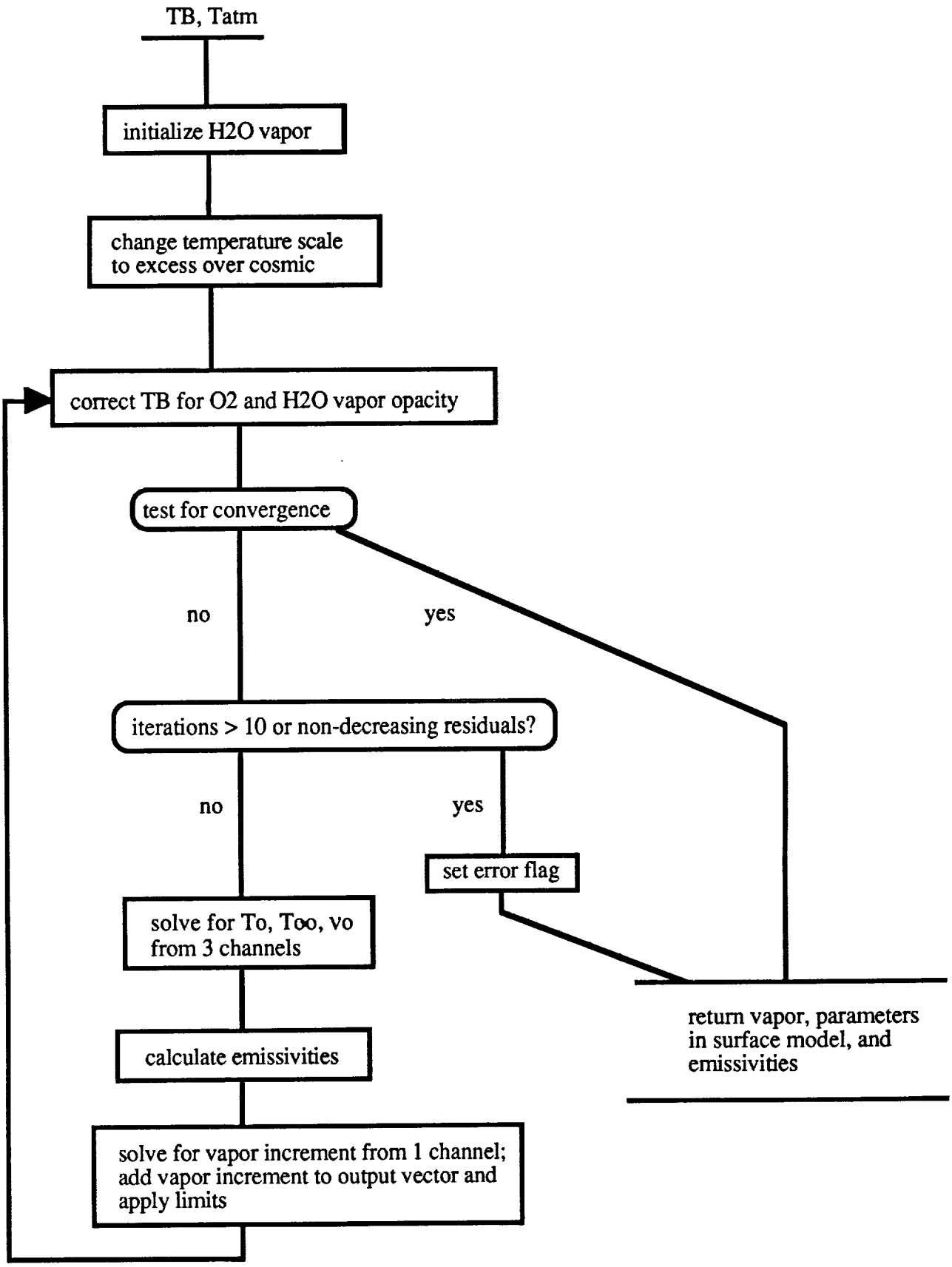

Figure 2.3. Cryosphere algorithm.

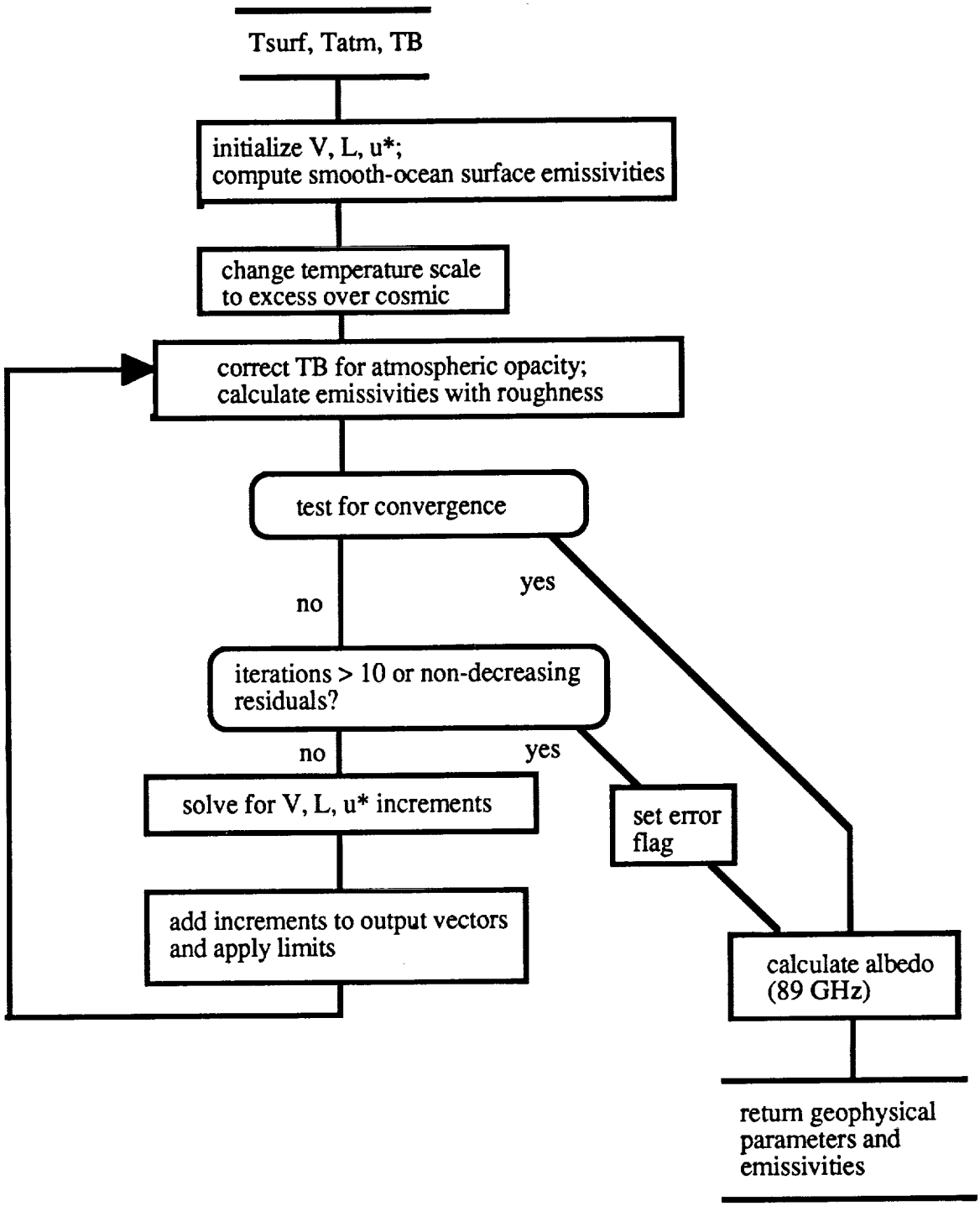

Figure 2.4. Hydrosphere algorithm.

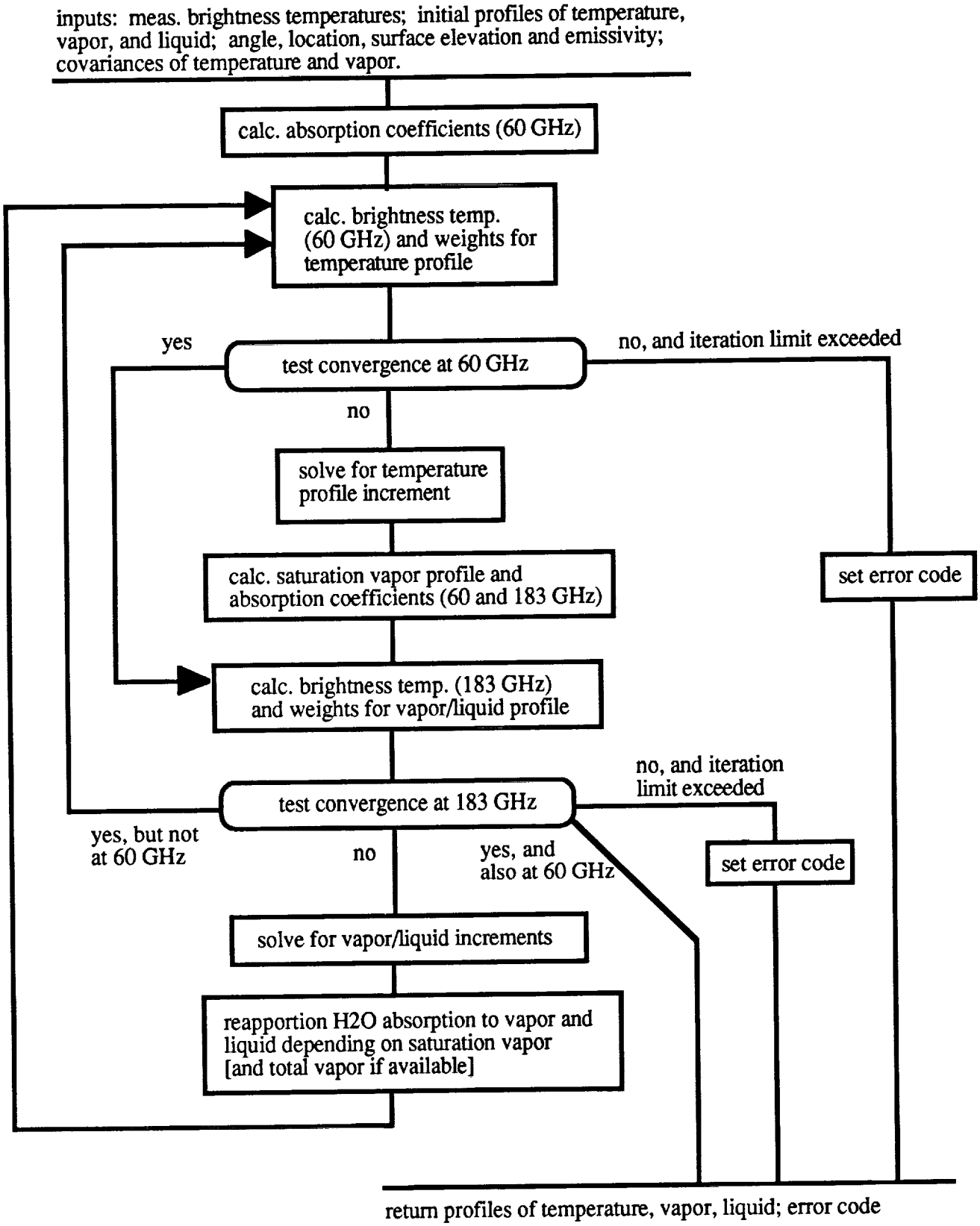

Figure 2.5. Profile retrieval algorithm.

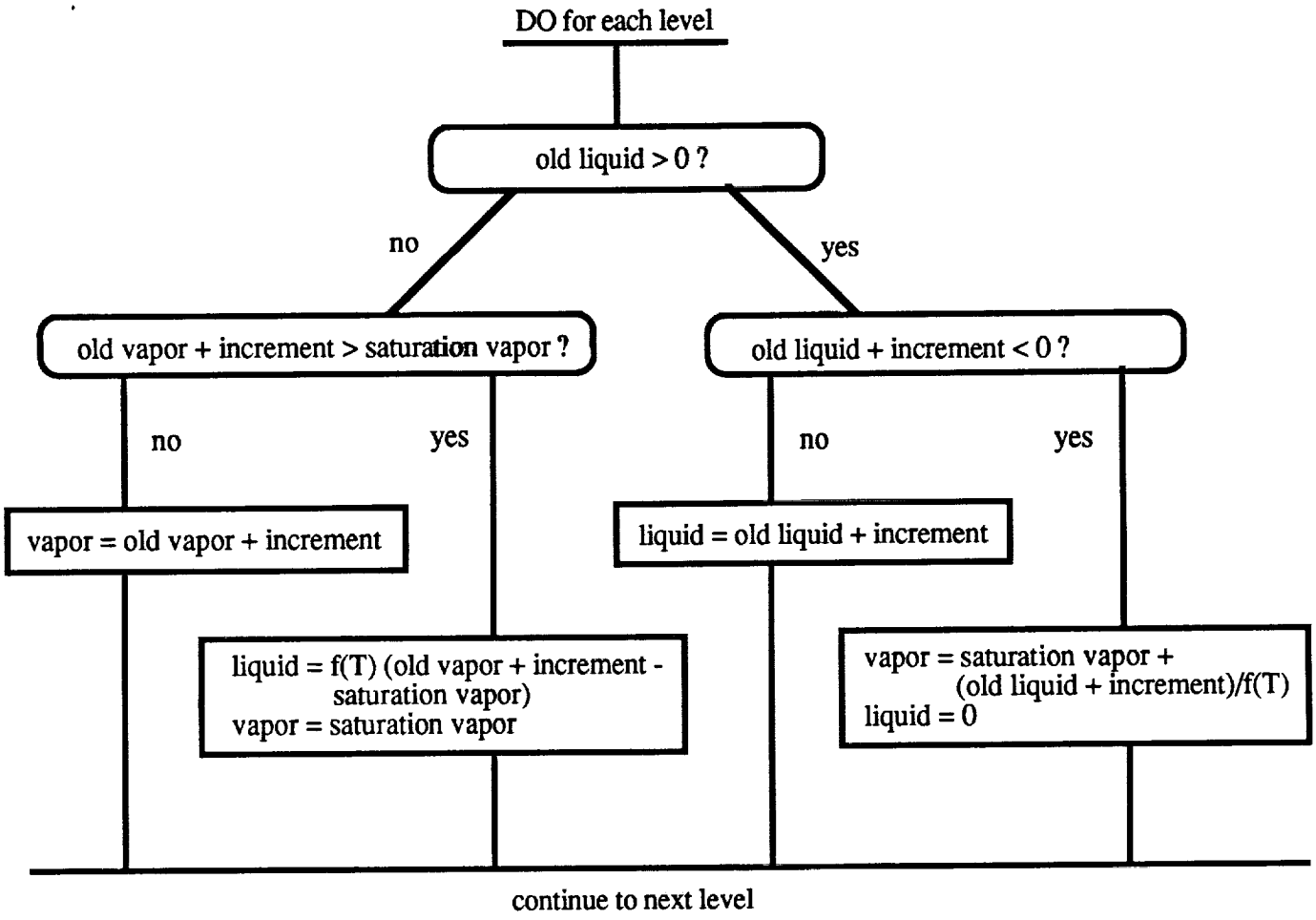

Figure 2.6. Reapportioning of H2O.

PRECIPITATION RETRIEVALS USING AMSU MICROWAVE OXYGEN-BAND DATA

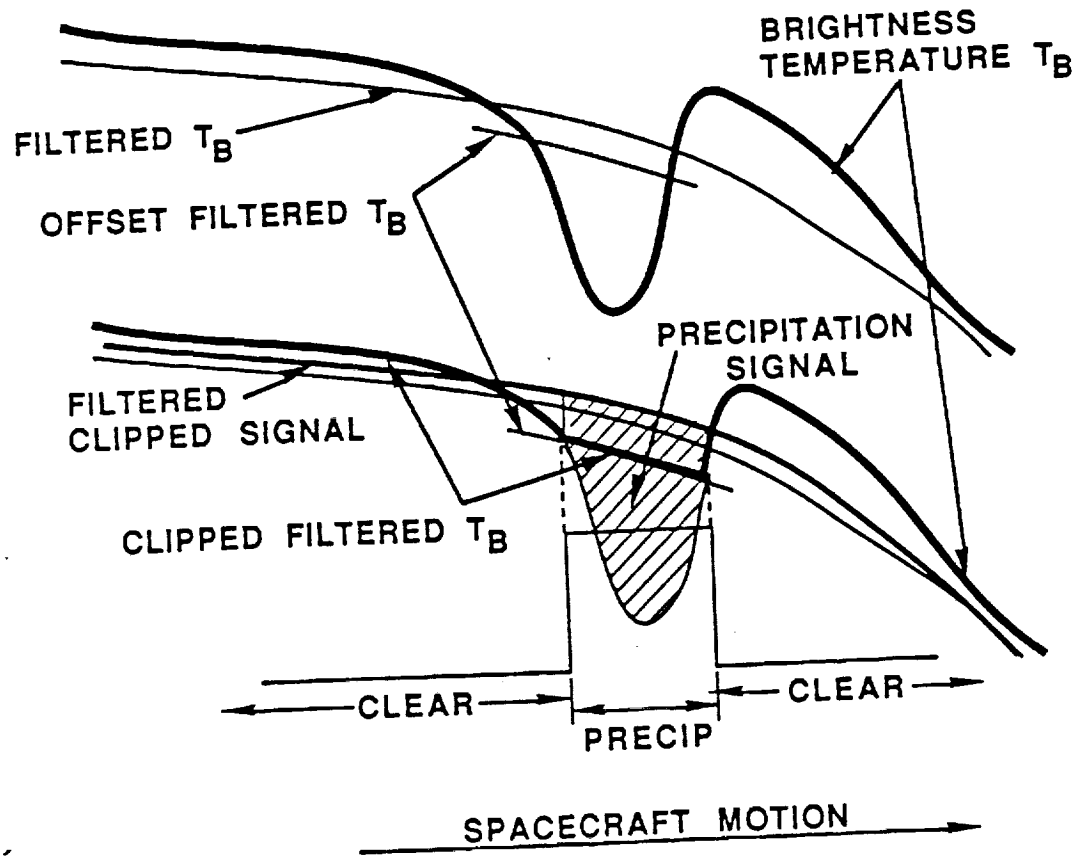

DHS-November 1991
Algorithm subject to change

Figure 2.7

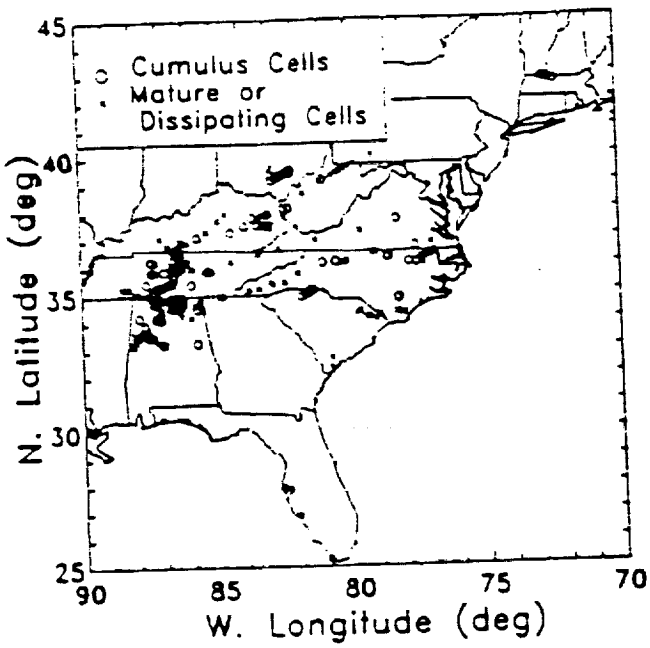

(a)

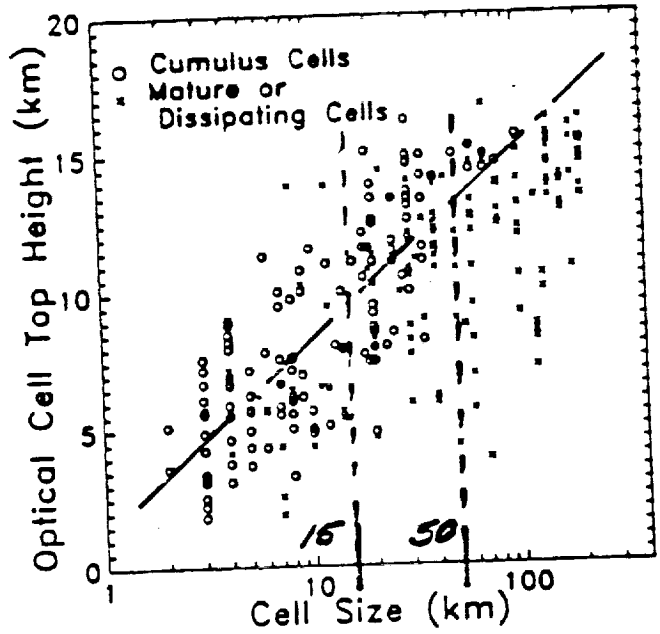

(b)

Figure 2.8(a) The locations of the 118-GHz rain cell observations during GALE and COHMEX. (b) Scatter plot of the optical cell top altitude a_i and cell size s_i for the 118-GHz rain cell observations. (Gasiewski, 1988)

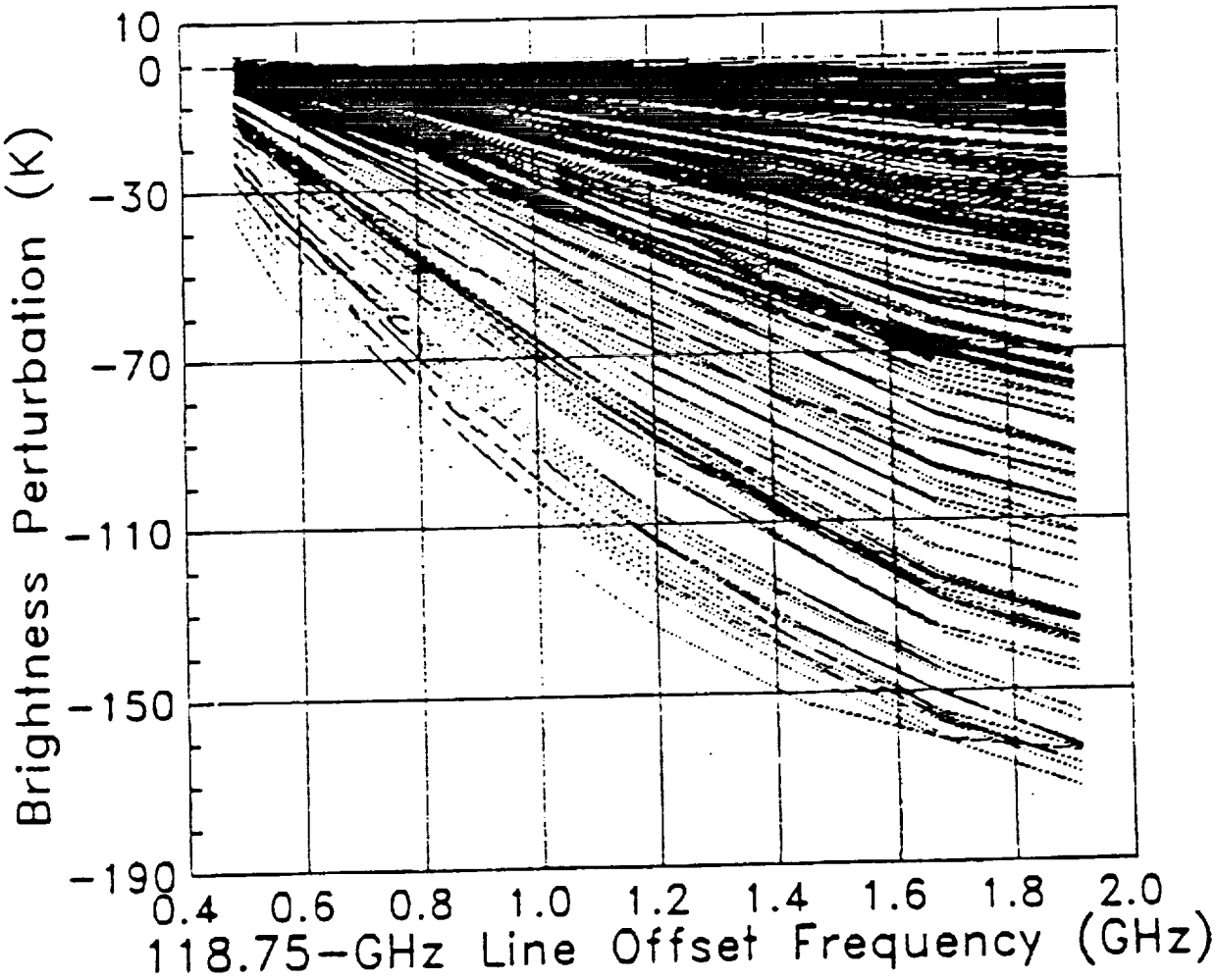

Figure 2.9 Ensemble of 118-GHz brightness temperature perturbation spectra observed by the MTS over cumulus, mature, and dissipating rain cells during GALE and COHMEX. (Gasiewski, 1988)

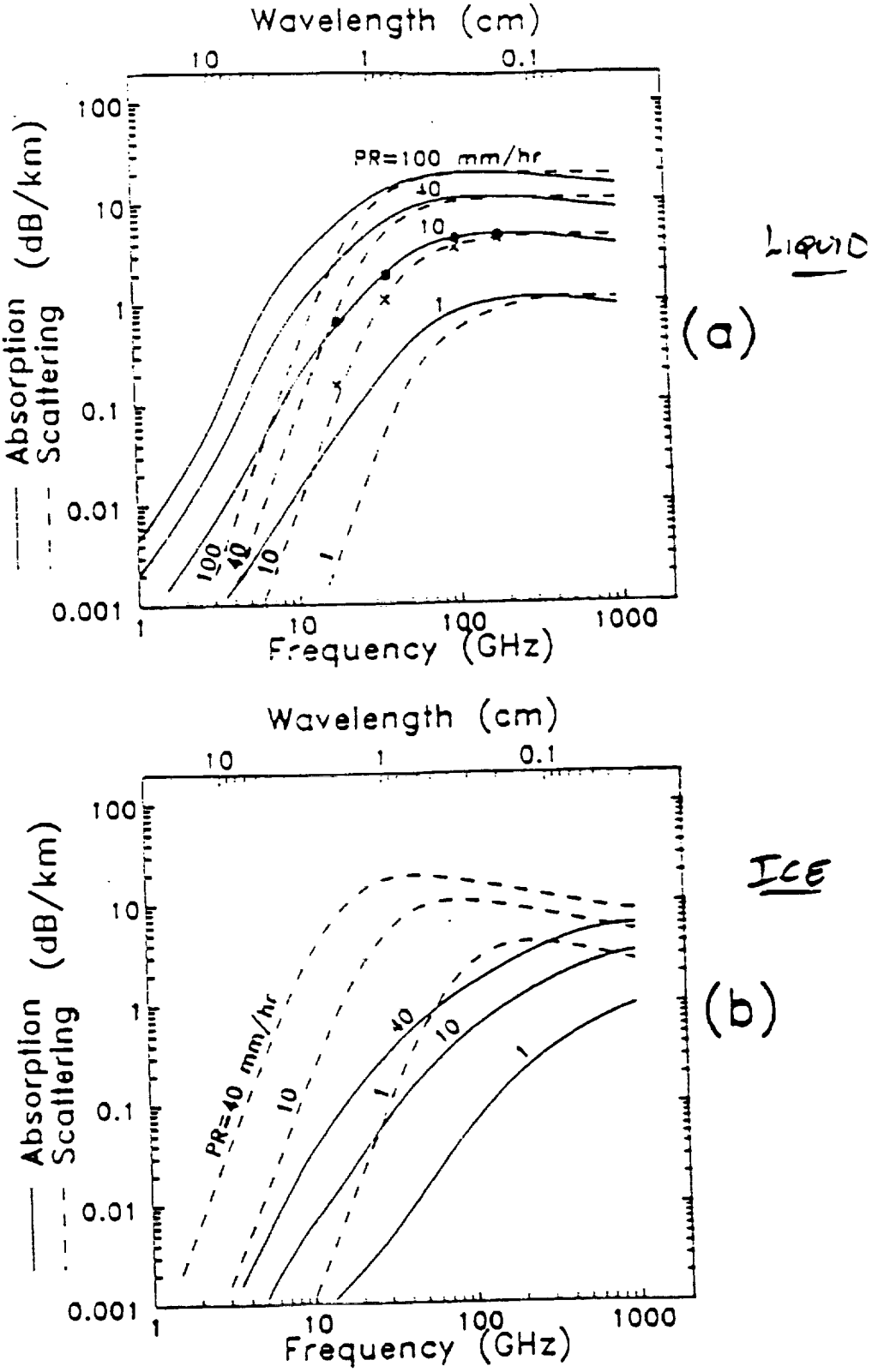

Figure 2.10 Polydispersive Mie hydrometeor absorption and scattering. (a) Liquid, assuming a Marshall-Palmer [1948] drop size distribution. Computations from Savage [1978] for absorption (•) and scattering (×) are plotted for comparison. (b) Ice, assuming a Sekhon-Srivastava [1970] distribution. Calculations are shown for precipitation rates of 1,10, and 40 mm/hr for both phases and 100 mm/hr for liquid. (From Gasiewski, 1988)

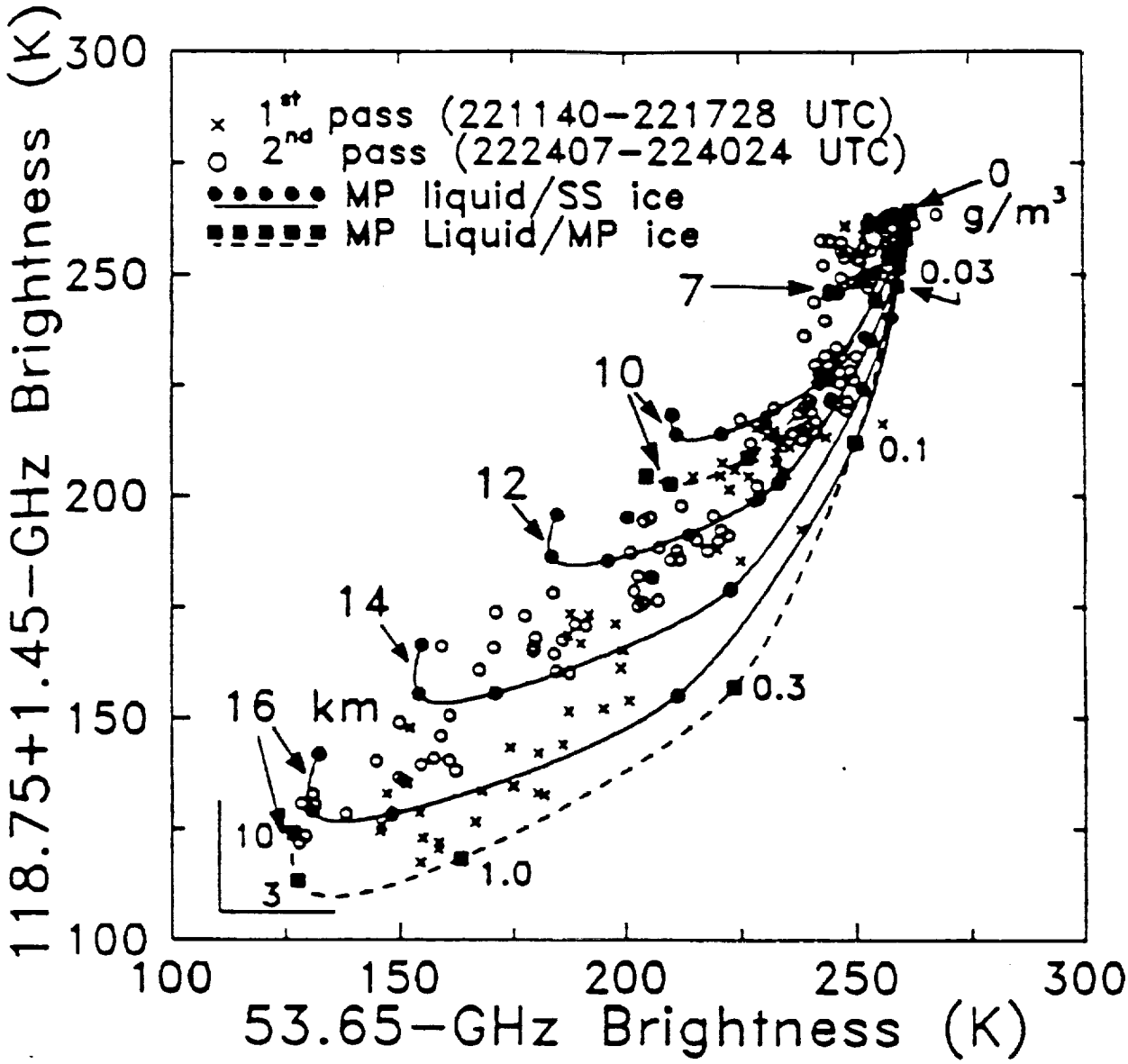

Figure 2.11 Brightness temperatures over precipitation for similar weighting function O_2 channels at 53.665 GHz and 118.75±1.47 GHz. The isolated points are MTS data observed during two passes over strong convection on June 29, 1986 during COHMEX. The solid lines are computed constant altitude curves parametrized by cell density. Computations used the A-D model with a Marshall-Palmer liquid size distribution and a Sekhon-Srivastava (solid) or Marshall-Palmer (dashed) ice size distribution. The crosshairs (lower left corner) indicate an offset added to the observed data for agreement with the computed brightnesses over hydrometeor-free regions. (Gasiewski, 1988)

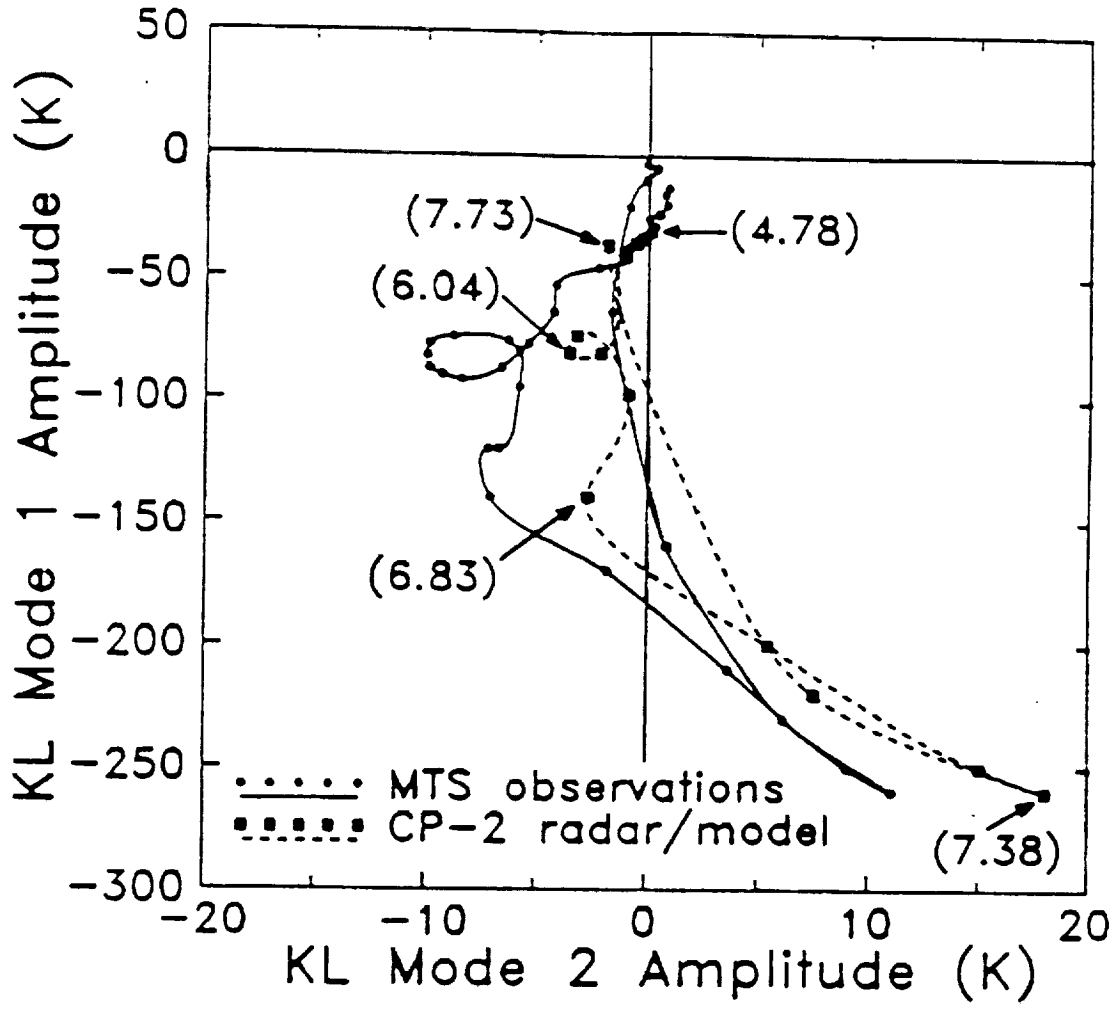

Figure 2.12 Trajectories of the two most dominant 118-GHz KL spectral coefficients (k_1 and k_2) for the precipitation cell couplet observed on July 11, 1986 during COHMEX: Nadiral radiometric brightness observations by the MTS (solid) and computations based on coincidentally observed CP-2 radar reflectivity using the iterative radiative transfer model described in the text (dashed). Selected times for computed points (indicated in parentheses) are in minutes after 2150 UTC. A computed-less-observed bias in k_2 of ~3 to 7 K is noted. (Gasiewski, 1988)

Figure 4.1

COMPARISON OF MIMR AND AMSU SPECIFICATIONS

MIMR[1] Freq. (GHz)	ΔTrms (K)	Footprint (km)	(km)	AMSU Freq. (GHz)	ΔTrms (K)	Footprint[2] (km)	(km)
6.8	0.15	39	60	NA			
10.65	0.37	25	38	NA			
18.7	0.50	14	22	NA			
23.8	0.43	13	20	23.8	0.3	50	50
36.5	0.44	8	12	31.4	0.3	50	50
90.0	0.70	3	5	89.0	0.5	50	50

Polarization

MIMR -- vertical and horizontal polarization

AMSU -- linear polarization at an angle of 90-θ degrees, where θ is the scan angle from nadir. At θ=90degrees, the polarization would be horizontal.

Angle of Incidence

MIMR -- 50° from zenith, at the ground

AMSU -- 0° to nearly 60°; estimate <35° for MIMR coincidence

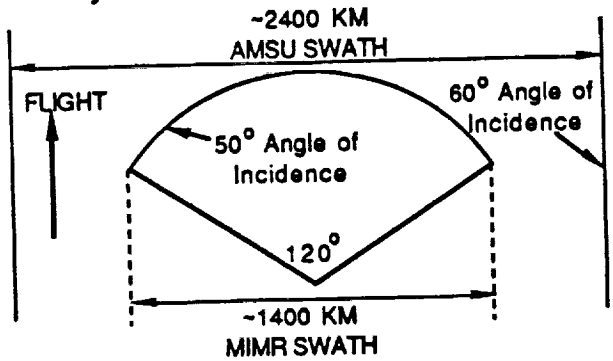

[1] Based on "The Multi-Frequency Imaging Microwave Radiometer - Instrument panel report", ESA SP-1138, August 1990.

[2] At nadir

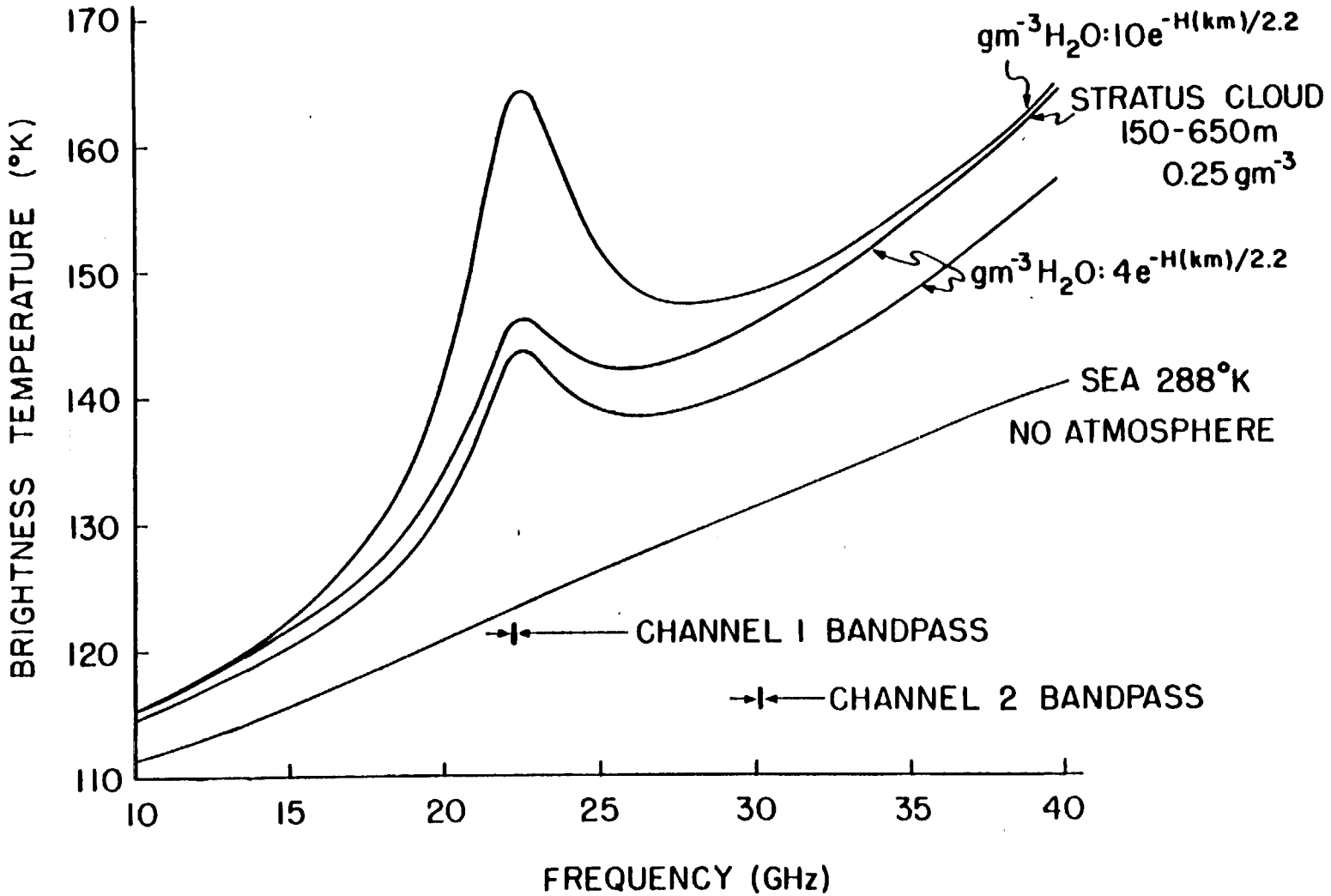

Figure 4.2 Brightness temperatures over a smooth ocean.

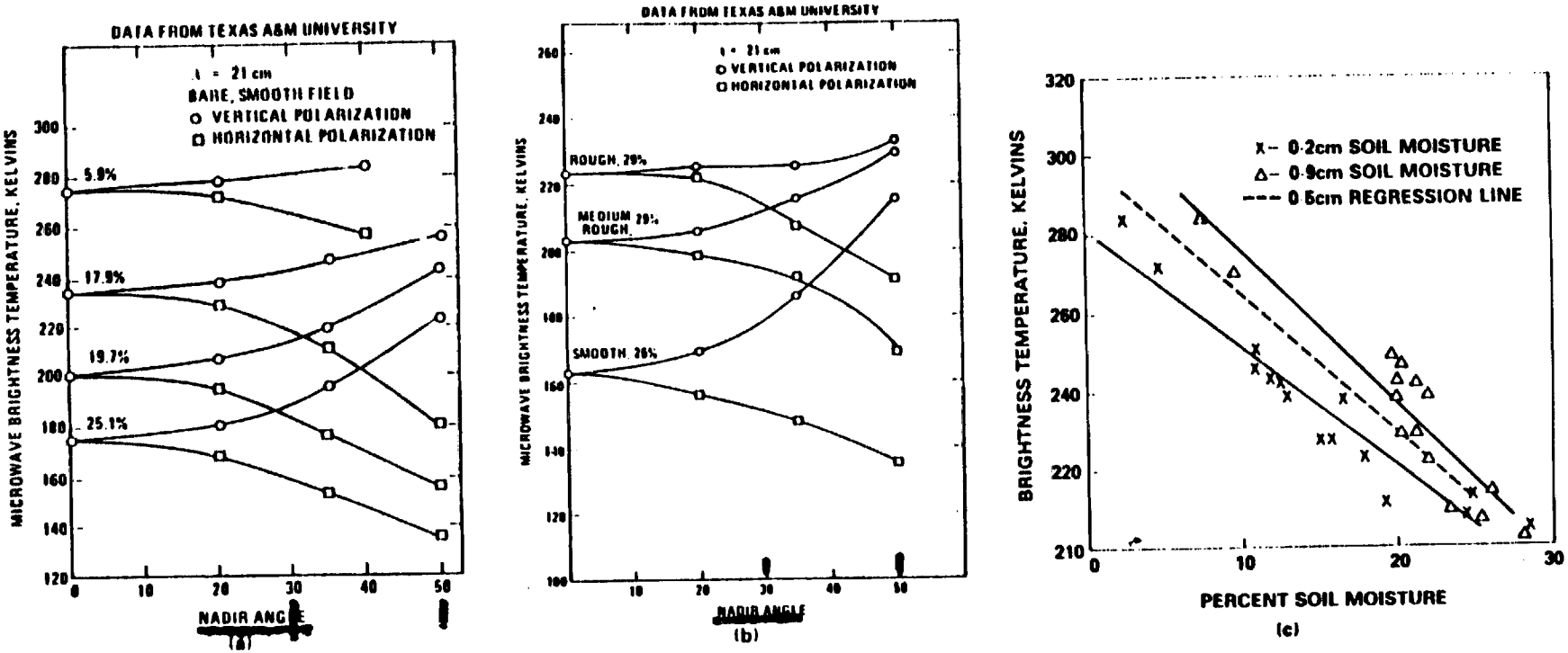

Figure 4.3 Results from field measurements performed at Texas A & M University: (a) T_B versus angle for different moisture levels; (b) T_B versus angle for different surface roughness at about the same moisture level; (c) T_B versus soil moisture in different layers for the medium rough field (Newton, 1976).

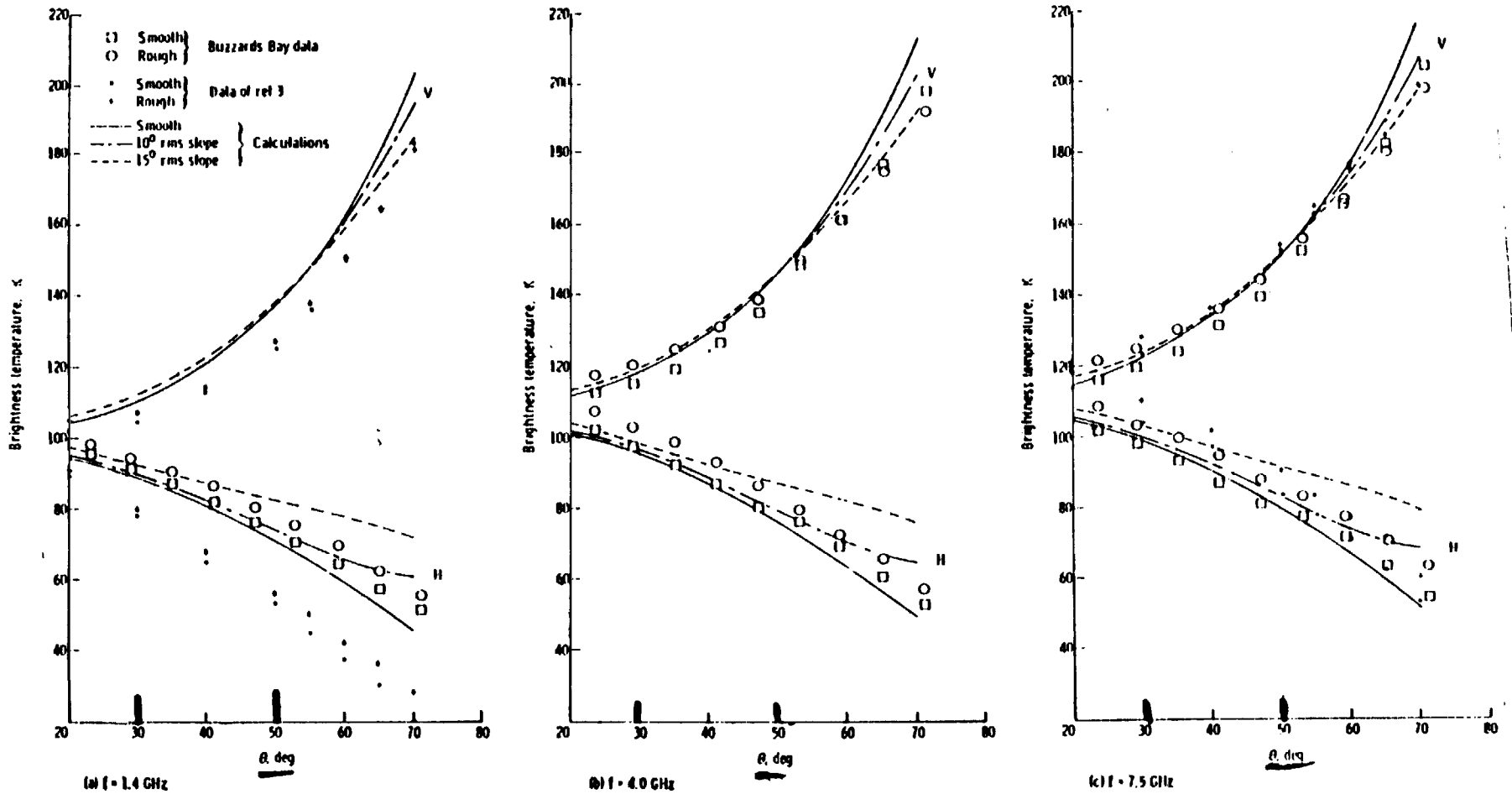

Fig. 4.4 Plots of radiometric brightness temperature vs. viewing angle. The calculations ar based on equations developed by Stogryn (1967) (V = vertical polarization, H = horizontal pola zation). The dots and crosses are data of Hollinger (1971).

NASA

Report Documentation Page

1. Report No.	2. Government Accession No.	3. Recipient's Catalog No.

4. Title and Subtitle
Advanced Microwave Sounding Unit Study for Atmospheric Infrared Sounder

5. Report Date
August 12, 1992

6. Performing Organization Code

7. Author(s)
Philip W. Rosenkranz and David H. Staelin

8. Performing Organization Report No.

10. Work Unit No.

9. Performing Organization Name and Address
Research Laboratory of Electronics
Massachusetts Institute of Technology
Cambridge, MA 02139

11. Contract or Grant No.
NAS 5-30791

13. Type of Report and Period Covered
Final
3/29/90-1/14/92

12. Sponsoring Agency Name and Address
NASA/Goddard Space Flight Center

14. Sponsoring Agency Code

15. Supplementary Notes

16. Abstract

The Atmospheric Infrared Sounder (AIRS), the Advanced Microwave Sounding Unit (AMSU-A) and the Microwave Humidity Sounder (MHS, formerly AMSU-B) together constitute the advanced sounding system facility for the Earth Observing System (EOS). This report is a summary of the EOS "phase B" activities of team members P. W. Rosenkranz and D. H. Staelin, through 1991. Work is continuing in the execution phase.

17. Key Words (Suggested by Author(s))	18. Distribution Statement
AIRS, AMSU, MHS	

19. Security Classif. (of this report)	20. Security Classif. (of this page)	21. No. of pages	22. Price
unclassified	unclassified	41	

NASA FORM 1626 OCT 86